Soft Robotics

A Soft Robotic Balloon Endoscope for Airway Procedures

Yingtian Li,[1,2,i] Joseph Peine,[1] Margherita Mencattelli,[1,ii] Jiaole Wang,[1]
Junhyoung Ha,[3] and Pierre E. Dupont[1,iii]

Abstract

Soft robots can provide advantages for medical interventions given their low cost and their ability to change shape and safely apply forces to tissue. This article explores the potential for their use for endoscopically-guided balloon dilation procedures in the airways. A scalable robot design based on balloon catheter technology is proposed, which is composed of five balloons together with a tip-mounted camera and LED. Its design parameters are optimized with respect to the clinical requirements associated with balloon dilation procedures in the trachea and bronchi. Possessing a lumen to allow for respiration and powered by the pressure and vacuum sources found in a clinical procedure room, the robot is teleoperated through the airways using a game controller and real-time video from the tip-mounted camera. The robot design includes proximal and distal bracing balloons that expand radially to produce traction forces. The distal bracing balloon is also used to perform balloon dilation. Three actuation balloons, located between the bracing balloons, produce elongation and bending of the robot body to enable locomotion and turning. An analysis of the actuation balloons, which incorporate helical coils to prevent radial collapse, provides design formulas by relating geometric parameters to such performance criteria as maximum change in actuator length and maximum robot bending angle. Experimental evaluation of a prototype robot inside rigid plastic tubes and *ex vivo* porcine airways is used to demonstrate the potential of the approach.

Keywords: medical robots, balloon dilation, robotic endoscope, airway management, endoluminal procedures

Introduction

BOTH ENDOSCOPES AND BALLOONS have found widespread use in minimally invasive medical procedures. In many endoluminal applications, such as in the airways and esophagus, they are used together to identify occluded regions and then to relieve the restriction through balloon dilation.[1–4] For example, in lung transplantation, occlusive scar tissue often forms at the site of the anastomosis between the patient's and donor's bronchi.[3] Similarly, surgery of the esophagus can often result in fibrotic occlusions that interfere with swallowing.[4] Endoscopically guided balloon dilation is the standard of care in both these situations.

[1]Department of Cardiovascular Surgery, Boston Children's Hospital, Harvard Medical School, Harvard University, Boston, Massachusetts, USA.
[2]Currently with Institute of Biomedical & Health Engineering, Shenzhen Institutes of Advanced Technology, Chinese Academy of Sciences, Shenzhen, China.
[3]Center for Medical Robotics, Robotics and Media Institute, Korea Institute of Science and Technology, Seoul, Korea.
[i]ORCID ID (https://orcid.org/0000-0001-7357-6535).
[ii]ORCID ID (https://orcid.org/0000-0002-4697-8923).
[iii]ORCID ID (https://orcid.org/0000-0001-7294-640X).

A common challenge of these procedures is the interference that occurs between the endoscope and the balloon. Since the balloon is inserted distally to the endoscope, the balloon partially blocks the endoscopic view leading to uncertainty in balloon positioning with respect to the tissue. In addition, occlusions in the lungs are often located around corners further increasing the challenges of visualizing balloon positioning, monitoring dilation, and inspection of the dilated tissue.

The objective of this article is to overcome these challenges by creating an endoscopic balloon-based robot that can propel itself through lumens, steer around corners, and perform balloon dilation. There are a number of additional desirable properties for such a robot. The design should be scalable to accommodate the anticipated range of lumen diameters in the airways. Specifically, for balloon dilations in the lungs, the robot should be able to navigate through the trachea (16 mm by 18 mm oval) and into the right main bronchus (35° turn, 13 mm inner diameter) and left main bronchus (43° turn, 11 mm inner diameter).[5] These are mean values across both sexes. Since the diameter varies somewhat along the length, these values are the maximum tracheal diameter and minimum main bronchi diameter.[5]

The robot should incorporate a central lumen not only to enable additional future functionalization but also to allow for respiration, as it travels through the lungs. To ensure adequate respiration, the lumen can be sized to approximate the inner diameter of an endotracheal tube (6–8 mm for women, 7–9 mm for men).[6] These tubes are used to keep the airway open during procedures such as bronchoscopies. It should also travel fast enough in body lumens to at least match existing endoscope advancement speeds of about 3 mm/s.[7] Furthermore, for clinical adoption, the robot should be fabricated from inexpensive biocompatible materials for single-use disposability and the system should be easy to operate. Finally, while the balloon pressures used for dilations in the airways can be up to 1 MPa,[8] it is preferable to use lower pressures for locomotion to reduce any chance of tissue damage and, owing to the compressibility of air, to maximize robot speed.

A significant number of soft robots that can locomote through tubes and body lumens have been reported.[9–22] These designs use a range of locomotion techniques, including inchworm[12,13,16,17] and peristaltic locomotion.[14,15] For example, Bernth et al. introduce an innovative technique to accommodate lumens of different diameters.[11] Rather than using an expanding design to press against the lumen walls, they bend the leading and trailing segments to create wall contact for traction. Connolly et al.[12] demonstrate a soft actuator technology combining an elastomeric matrix and inextensible fibers to create an inchworm robot, which crawls through a curved plastic tube. Zhang et al. demonstrate a 15 mm diameter inchworm robot that can navigate a branching network of tubes.[17] The technologies described in Takeshima and Takayama and Ozaki et al.[13,14] use surface travelling waves generated by periodic inflation of tubular actuators helically wound around the robot body.

A subset of these soft robots have been designed for endoscopic use and, in particular, for use inside the colon.[9,10,18,19,20] With the mean colon diameter varying between 26 and 47 mm based on location,[23] these robots are significantly larger than what is needed for the airways. They

do, however, provide data for which locomotion techniques will be effective inside slippery compliant body lumens. Some of these articles use bracing balloons to press against opposing walls of the colon.[18–20] Because the bowel walls are highly elastic (much more so than the airways), alternative techniques such as swimming[9] and attaching to a specific wall location[10] using suction have been developed.

These robots each introduce novel capabilities; however, they do not fully satisfy the clinical constraints enumerated above. Locomotion speed is typically low. For example, a maximum speed of 1.21 mm/s in a simulated colon was achieved.[11] Many designs lack a central lumen. And while most designs can achieve the desired turning angles, their design complexity increases manufacturing costs.

In this article, we present and evaluate the first inchworm balloon endoscope designed for inspection and balloon dilation of the airways. To provide a clear pathway to regulatory approval and commercialization, we used materials and techniques that can be adapted to those used by the medical balloon-catheter industry. The resulting prototype robot, sized for use in the trachea and bronchi, is inexpensive (robot <$5.00, optical system $126, reusable controller $213). Furthermore, it is designed to be powered by the pressure and vacuum lines available in a medical procedure room.

While prior balloon-based robot designs have typically been fabricated from elastic materials such as silicone, we constructed our balloons from thin plastic membranes which are relatively inelastic. This approach provides two advantages. First, the balloon material does not need to be stretched during inflation. This is comparable to how many medical balloon catheters are constructed and it means that the same volume change can occur at a lower inflation pressure. Furthermore, since the bracing balloons have a lumen, their volume is smaller compared to a solid cylindrical balloon and so can be filled and emptied faster resulting in faster walking speeds.

The article includes several analytical contributions. First, while propulsion balloons with internal helical springs have been previously proposed, we have derived the optimal value of spring pitch to maximize actuator stroke while preventing radial collapse and have also provided an analytical expression for robot balloon twisting. In addition, we derived the maximum turning angle for the robot using an energy minimization technique.

The remainder of the article is arranged as follows. In the following section, the design and fabrication process are described. We then provide a detailed analysis which relates the design parameters to robot performance specifications such as maximum bending angle and robot speed. These analyses are then verified experimentally. Next, robot navigation is demonstrated in an *ex vivo* swine trachea. Finally, conclusions are presented.

Materials and Methods

Robot design

Our goal was to develop a simple scalable design that could be constructed using balloon catheter manufacturing techniques. The laboratory-constructed prototype presented here is sized for use in the trachea and main bronchi. The proposed robot is composed of three segments: a distal bracing balloon, a middle actuation balloon segment, and a proximal bracing balloon. As shown in Figure 1A, a camera
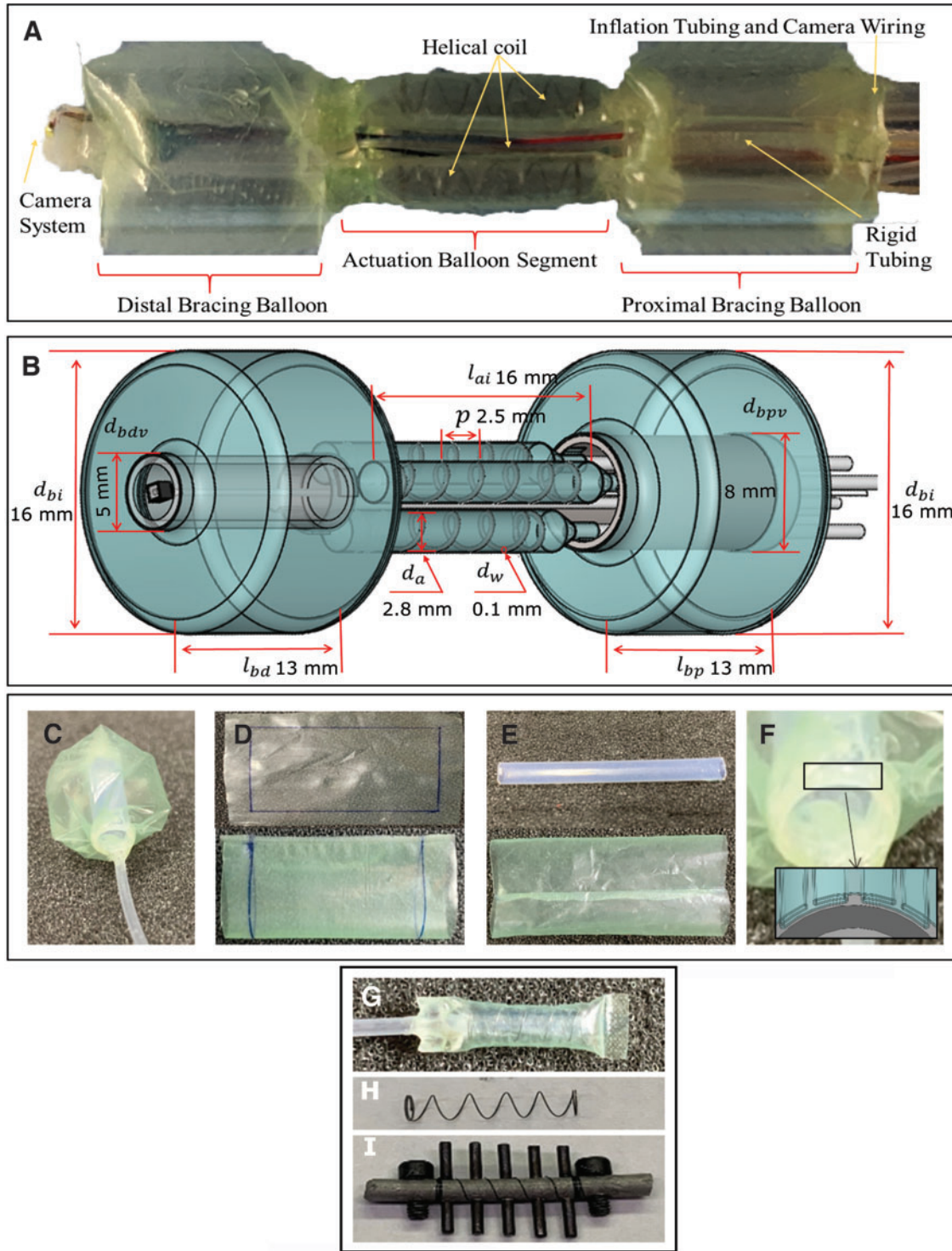
FIG. 1. Robotic balloon endoscope design and fabrication. **(A)** Robot prototype. **(B)** Design parameters. **(C)** Inflated bracing balloon. **(D)** Formation of cylindrical membrane from sheet stock is first step in fabrication of both bracing and actuation balloons. **(E)** Bracing balloon is assembled by gluing ends of inverted membrane cylinder on section of rigid polymer tube. **(F)** Membrane is pleated at ends to enable gluing to tube. **(G)** Actuation balloon composed of cylindrical balloon with internal helical NiTi coil. Balloon ends are sealed flat for attachment to bracing balloon tubes. **(H)** Helical NiTi coil. **(I)** Fixture for shape setting NiTi wire. Color images are available online.

TABLE 1. NOMENCLATURE AND PROTOTYPE PARAMETER VALUES

Description	Variable	Prototype value
Inflated diameter of bracing balloons	d_{bi}	16 mm
Vacuum (deflated) diameter of proximal bracing balloon	d_{bpv}	8.1 mm
Lumen diameter of proximal bracing balloon	d_{bpl}	7.9 mm
Vacuum (deflated) diameter of distal bracing balloon	d_{bdv}	5.2 mm
Lumen diameter of distal bracing balloon	d_{bdl}	5.0 mm
Length of proximal bracing balloon	l_{bp}	13 mm
Length of distal bracing balloon	l_{bd}	13 mm
Length of inflated actuation balloons	l_{ai}	16 mm
Length of vacuum (deflated) actuation balloons	l_{av}	10 mm
Change in length of actuation balloons	$\Delta l = l_{ai} - l_{av}$	6.1 mm
Maximized change in length of actuation balloons	Δl^*	6.1 mm
Diameter of individual actuator balloon	d_a	2.8 mm
No. of helical coils in inflated actuator balloon	n_i	4.5
No. of helical spring coils in actuator balloon under vacuum (deflated)	n_v	4.64
Pitch of helical coil in inflated actuation balloon (*=optimal)	p_i	2.5 mm
Pitch of compressed helical coil in actuation balloon (*=optimal)	p_v	0.3 mm
Helical coil wire diameter	d_w	0.1 mm
Thickness of balloon membrane	t	0.1 mm
Length of wire comprising helical coil	l_w	58.8 mm
Angle of twist as helical coil is compressed	φ	45°
Bracing balloon inflation and deflation times	t_{bi}, t_{bv}, t_b	Varying
Actuation balloon inflation and deflation times	t_{ai}, t_{av}, t_a	0.16 s, 0.16 s, -

system is attached to the distal segment. Figure 1B and Table 1 define the geometric design parameters that will be used in the article.

The inchworm robot is made from inexpensive materials as detailed in Supplementary Table S1 of the Supplementary Data. Biocompatible versions of all materials used in the robot are available. As with medical dilation balloons, an inelastic polymer is selected to fabricate all the five balloons so that they will retain their size and shape under pressure. In addition, in similarity with medical balloons, both positive and negative pressure differentials with respect to atmospheric pressure are used to control expansion and contraction, respectively.

Distal and proximal bracing balloons

As the head and tail of the robot, the proximal and distal bracing balloons are made of plastic membranes which expand around the circumference of rigid polymer tubes. The balloon/tube sections are toroidal in shape and leave the inner lumen of the tube open as shown in Figure 1C. This design provides several advantages. The inner tube reduces the inflation volume of the balloon leading to faster inflation and deflation times. Furthermore, the inner lumen provides a passage both for respiration and for connections to the imaging system. In particular, a miniature camera (NanEye, ams and OSRAM) is mounted in the lumen of the distal bracing balloon.

The first step of balloon fabrication is to form a membrane cylinder by heat sealing two edges from a rectangle cut from sheet stock (Fig. 1D). The cylinder is then turned inside out so that the sealed edge will be located in the balloon interior and the ends of the cylinder are glued to the ends of the tube (Fig. 1E, F). For gluing the ends of the membrane cylinder are folded using the

pattern shown in the inset of Figure 1F. Inflation tubing is integrated during this step to produce the result shown in Figure 1C.

Actuation balloons

The actuation segment is composed of three linearly expanding balloons (Fig. 1G), which provide propulsion and 3D steering capability to the robot. Each balloon contains an internal helical coil (Fig. 1H). While combinations of balloon actuators or air channels are widely used as expanding and bending actuators,[19,21,22] the design described here has several novel features. First, similar to the innovative design of Ref.,[21] the internal helical coil ensures that balloon deflation produces linear contraction rather than radial collapse. This enables that the pitch of the helix can be selected so as to minimize the deflated length (Selecting Helical Pitch to Maximize Balloon Shortening section). Furthermore, rather than relying on the internal springs to produce balloon expansion,[21] we design the springs to be weak in axial compression and use both positive and negative pressure differentials for actuation to maximize propulsion speed. Using positive pressures enables the expanded balloons to resist bending and buckling so as to produce larger robot bending angles (Maximum Robot Bending Angle section).

The fabrication of each actuation balloon also starts by preparing a cylindrical membrane (Fig. 1D). Initially, we fabricated helical coils using a 3D printed polymer, but we found that the coils would fail due to fatigue and so we switched to making the coils from NiTi wire. The helical coil is shape set from super-elastic NiTi wire (0.004 in diameter) by clamping it on fixture as shown in Figure 1I, baking it at 525°C for 20 min and then quenching it in water. The coil is then inserted into the cylinder, and the two ends are heat
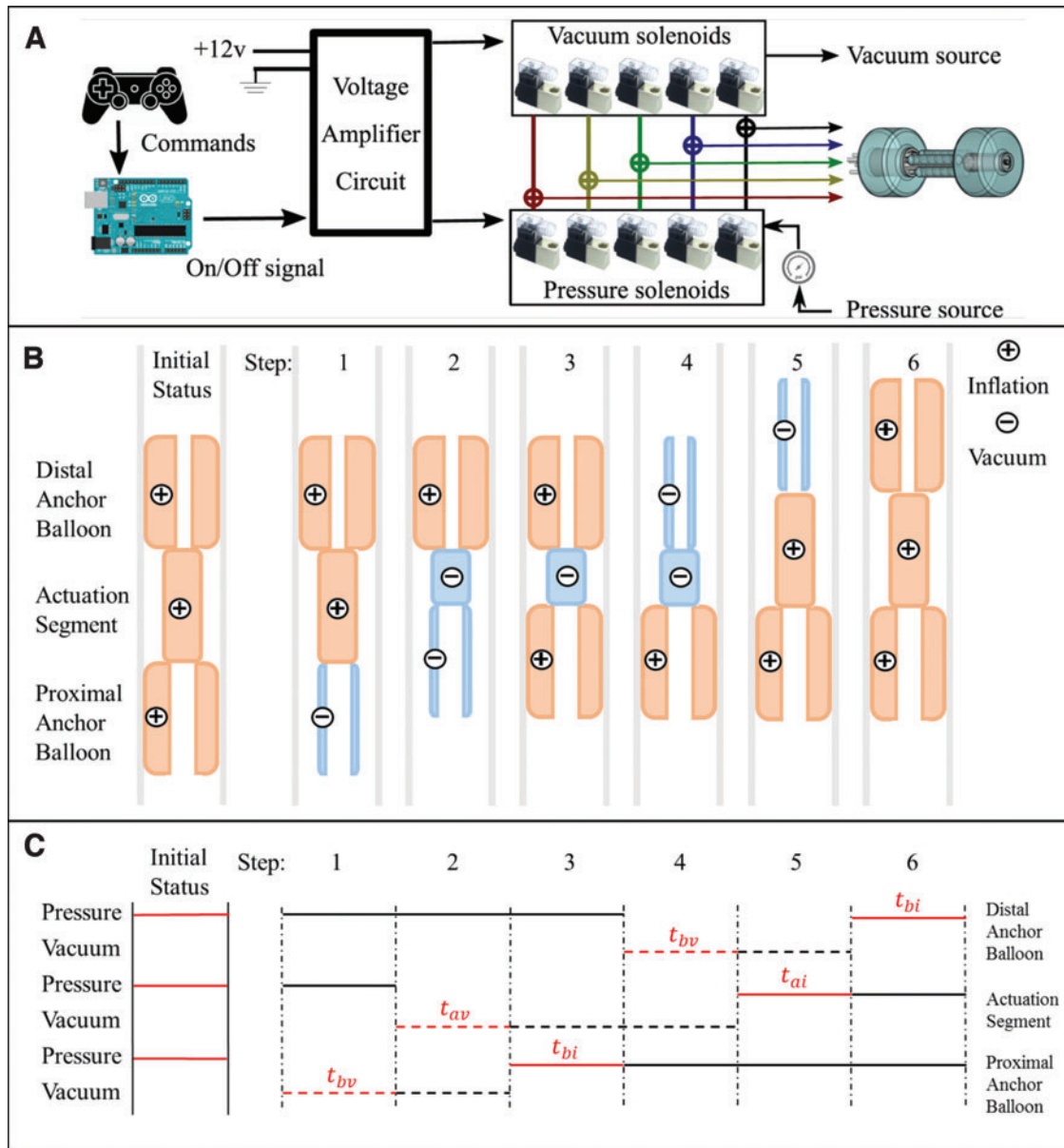
FIG. 2. Robot controller. **(A)** Control system schematic. **(B)** Six-step locomotion sequence. **(C)** Balloon inflation and deflation timing for locomotion. The {inflation, deflation (vacuum)} timing parameters of the actuation and bracing balloons are, respectively, $\{t_{ai}, t_{av}\}$ and $\{t_{bi}, t_{bv}\}$. These time intervals represent the head start that each step has before the next step is initiated. The pressure and vacuum solenoids only switch at the beginning of these intervals. In this way, the balloons are connected to the full supply or vacuum pressure up until the moment they switch from supply to vacuum pressure or vice versa. This approach makes the robot more resilient to any leaks that may occur in the balloons. Color images are available online.

sealed to produce the balloon of Figure 1A. Since the balloon's membrane is very thin, the effective balloon diameter and length are the same as those of the helical coil.

Robot assembly and control

To assemble the robot, the actuation balloons are arranged 120° apart around the circumference of the tubes comprising the cores of the anchor balloons. They are then glued to the insides of the tubes. A CMOS camera and two LEDs, mounted in a 3D printed frame, are affixed to the end of the distal bracing balloon. All the inflation tubing (inner diameter

1 mm) and connecting wires (16 gauge) for the LED and camera pass through the inner lumens of the bracing balloons and between the actuation balloons.

As shown in Figure 2A, the robot is operated using a PS2 game controller with the buttons of the controller programmed to enable inflation/deflation of individual balloons, as well as to control coordinated inflation/deflation sequences, which produce forward motion, backward motion, and forward turning in 3D.

A microprocessor (Arduino) is programmed to convert the PS2 button commands into sequences of inflation and deflation commands represented as $\{0, 5\}$ V signals. Pairs of

solenoids (AOMAG) are used to control inflation and deflation of each balloon. Pressure and vacuum sources, comparable to what is available in clinical procedure rooms, were used to power the robot. The pressure source was connected to a regulator to reduce inflation pressure to a specified value. Tests with *ex vivo* porcine tracheas showed that inflation pressures of 34.5 k–55 Pa did not visibly damage the tissue. The full vacuum pressure of −62 kPa was used for deflation. A voltage amplifier circuit converts the $\{0,5\}$V signals from the microprocessor to the $\{0,12\}$V signals required by the solenoids.

Motion control

The inflation/deflation sequence for forward motion is shown in Figure 2B. Starting with all five balloons inflated, the 6-step sequence consists of sequentially deflating the proximal bracing balloon and then the three actuation balloons, inflating the proximal bracing balloon, deflating the distal bracing balloon, and then inflating the three actuation balloons followed by the distal bracing balloon. The corresponding inflation and deflation timing sequence is given in Figure 2C. Timing duration parameters are investigated experimentally later in the article.

To perform turning of the distal section for visualization of the workspace or for navigating around a corner, the proximal bracing balloon is inflated, and the distal bracing balloon is deflated. Differential inflations and deflations are then applied to the three actuation balloons to achieve the desired bending angle. For navigating around a corner, once at the desired angle, the distal bracing balloon is inflated to lock in the tip direction.

Design Analysis

The robot's design parameters are shown in Figure 1B and Table 1. Robot design involves selecting parameter values that optimize robot performance for a specific application. As described in the introduction, the important specifications for endoscopic and balloon dilation procedures include the following.

1. The robot should incorporate a central lumen to enable respiration, drainage, and imaging system wiring.
2. The design should be sized for the anticipated range of lumen diameters and for the targeted balloon dilation diameter.
3. Its speed should be comparable to endoscope advancement speeds.
4. Its maximum turning angle should match clinical requirements.

The first specification follows from the tube-based design of the bracing balloons. The space between and around the three actuator balloons is connected to the lumens of the two bracing balloons creating a continuous passage through the robot body.

To meet the third specification, it is necessary to model the relationship between the robot design parameters and its maximum propulsion speed. The fourth specification requires a parameter-based model of the maximum turning angle. These models are developed in the following subsections.

Bracing balloon design

The design parameters of the bracing balloons are selected based on specifications 2–4. Tube diameters d_{bpv} and d_{bdv} control balloon minimum diameter. We wish to select these values to be as large as possible for respiration, as well as to minimize bracing balloon fill/vacuum time (so as to maximize speed); however, larger values also limit the minimum diameter lumen that can be entered. Maximum inflated diameters d_{bi} should be selected just large enough to obtain sufficient propulsive gripping force. Larger diameters are not as compact when deflated and so increase effective minimum deflated diameters.

Balloon diameter. To create a prototype sized for the human trachea and bronchi, the bracing balloons must accommodate the inner diameters of the trachea (16 mm by 18 mm oval), right main bronchus (13 mm), and left main bronchus (11 mm).[5] This requires spanning the diameter range of 11–16 mm. These values indicate that the balloon tubing outer diameters must be <11 mm with an inner diameter of 7–8 mm for respiration to match endotracheal tubes.

Similarly, the maximum balloon diameter must be larger than 16 mm, for example, 17 mm. We wished to test our prototype, however, in smaller *ex vivo* porcine airways in which the tracheal diameter is about 12 mm and the bronchi diameters are about 9 mm.

As a compromise, we selected the proximal and distal bracing balloon tube outer diameters, d_{bpv} and d_{bdv}, to be 8.1 and 5.2 mm, respectively. Thus, the proximal balloon tube diameter matches the size indicated by human airway dimensions, while the distal balloon tube diameter is sized for porcine airway dimensions. The goal of this choice was to enable us to demonstrate the robot at human airway scale while allowing at least the head of the robot to enter the porcine bronchi. Recalling that larger balloons have larger deflated diameters, we also selected the inflated diameter of the bracing balloons to be 16 mm to ensure at least partial entry into the porcine bronchi. This value is less than the desired value of 17 mm for the human trachea, but exceeds what is required for the human bronchi. Thus, our design should be capable of navigating through tubes with inner diameters ranging from 11 to 15 mm.

The corresponding bracing balloon lumen diameters were 7.9 and 5.0 mm for the proximal and distal bracing balloons, respectively. The lumen size of the proximal balloon matches the desired endotracheal lumen diameter of 7–8 mm, while the distal balloon lumen has been reduced in the prototype to enable navigation of the porcine bronchi.

Balloon length. In selecting the lengths of the bracing balloons l_{bp} and l_{bd}, we note that reducing balloon length decreases the filling and vacuum times and so increases robot speed. As balloon length becomes shorter than inflated diameter, however, the balloon may deflate longitudinally under vacuum before deflating radially. Consequently, we found that the minimum practical length of the anchor balloon is only slightly less than the inflated length. Given balloon inflation diameters of 16 mm, we selected a balloon length of 13 mm to achieve minimum volume without risking longitudinal collapse.

Actuation balloon design

The design parameters of the actuation balloons are selected based on specifications 3 and 4 relating to robot speed and maximum turning angle. Both robot speed and maximum turning angle are dependent on the maximum balloon lengths l_{ai} and the change in the actuation balloon length under vacuum Δl. Speed also depends on actuation balloon diameter d_a since reducing diameter reduces fill and vacuum times. We assume that balloon widths are sufficiently small that they do not interfere with each other and so affect turning angle.

To develop a design process for the actuation balloons, we first model below a single balloon to understand how the internal helical coil affects its behavior under vacuum. In particular, expressions are developed relating balloon diameter and coil pitch to maximize the change in the balloon length, $\Delta l = l_{ai} - l_{av}$. This involves three steps. We first show how to select coil pitch to maximize balloon shortening under vacuum. Next, we develop an expression for the twisting and change in the number of coils that occurs as the balloon shortens. These are combined in the third step to provide an expression for maximum change in balloon length. In the following subsections, we then develop expressions for the dependence of speed and turning angle on maximum balloon length and its length change.

Selecting helical pitch to maximize balloon shortening.

The purpose of the internal coil is to ensure that, under vacuum, the balloon compresses longitudinally rather than radially. If the pitch is selected to be too large, then the balloon can collapse radially between the coils and so prevent further decrease in length. If the pitch is selected to be very small, however, adjacent coils will contact each other and so prevent further longitudinal shortening of the balloon. Thus, the goal is to select the pitch of the coil such that radial collapse of the membrane between the coils occurs at the same time as longitudinal contact between adjacent coils. This condition maximizes the change in length per unit inflated length of the actuation balloon and is illustrated in Figure 3A and B.

When inflated, the axial length of the membrane between coils is p_i as shown in Figure 3A. Experimentally, it is observed that, under vacuum, the balloon stops reducing in length when opposing folds on the membrane come into contact and block air flow. To achieve the maximum change in length, this should not occur until the coils themselves are about to touch as illustrated in Figure 3B. In this state the lengths of membrane p_i from each side of the coil touch in the center. The geometric relationship between coil pitch and diameter can be approximated by:

$$p_i = 2\left(\frac{d_a - d_w}{2} + \frac{\pi d_w}{4}\right) = d_a + d_w\left(\frac{\pi}{2} - 1\right). \quad (1)$$

Since $d_a \gg d_w$, Equation (1) can be simplified so that optimal design pitch p_i^* is selected as:

$$p_i^* = d_a. \quad (2)$$

Given this optimal value of pitch when the balloon is fully expanded, the pitch at full compression p_v^* will be given by:

$$p_v^* = d_w + 2t. \quad (3)$$

As the coils compress from a pitch of p_i^* down to p_v^*, the coil diameter remains constant, but the number of coils increases and the ends of the coils twist with respect to each other. These quantities are computed in the subsection below.

Change in coil number and balloon twisting during shortening.

As the helical coil compresses longitudinally, it twists in a manner that preserves coil diameter and wire length. The wire length l_w can be computed using the geometric expression for a helix to be:

$$l_w = n\sqrt{(\pi d_a)^2 + p^2}. \quad (4)$$

Equating wire lengths for pressurized and compressed lengths yields an expression relating the number of coils in each state given by
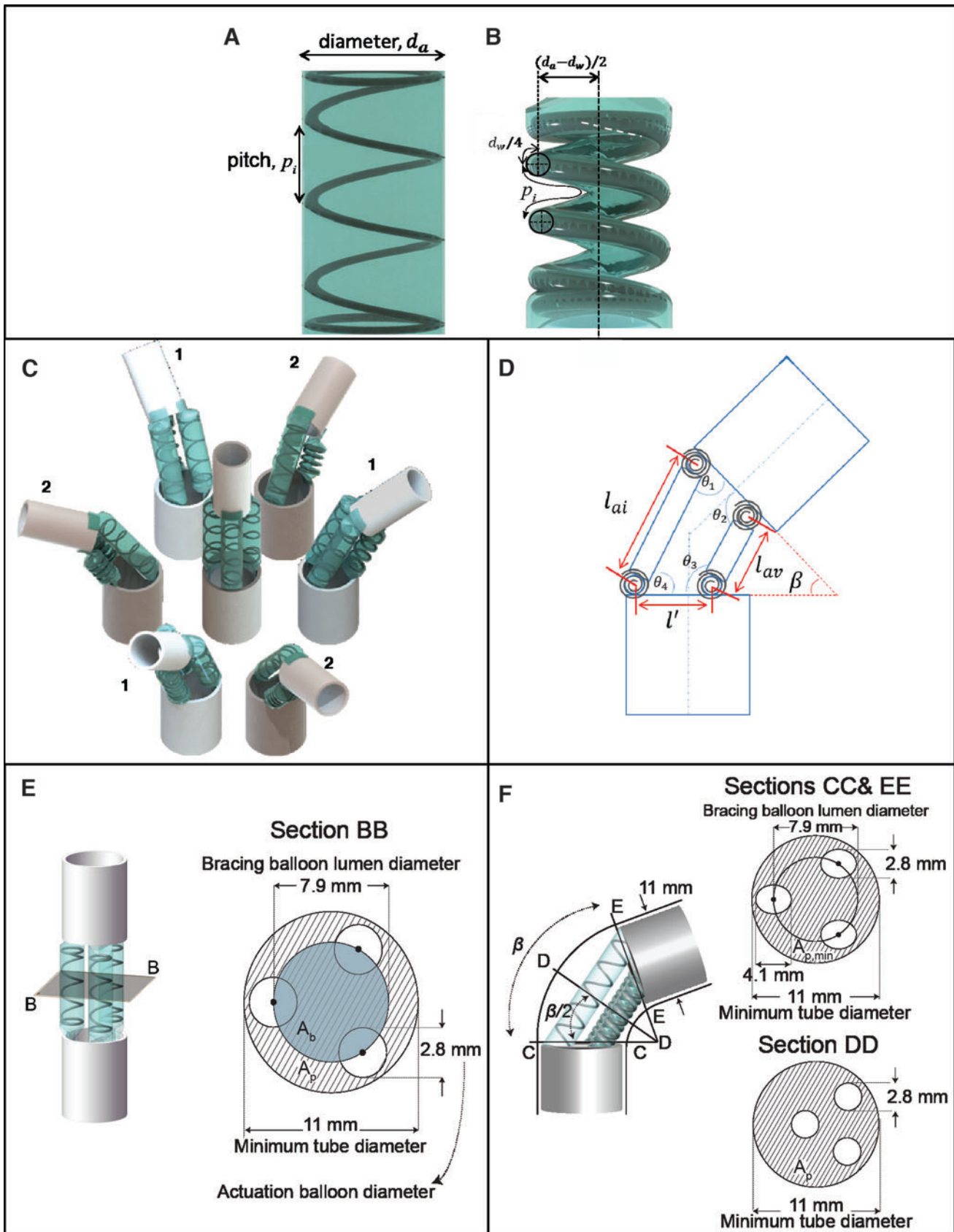
$$n_v = n_i\sqrt{\frac{(\pi d_a)^2 + p_i^{*2}}{(\pi d_a)^2 + p_v^{*2}}}. \quad (5)$$

We can now compute the twist of the coil and actuation balloon as:

$$\varphi = 2\pi(n_v - n_i) = 2\pi n_i\left(\sqrt{\frac{(\pi d_a)^2 + p_i^{*2}}{(\pi d_a)^2 + p_v^{*2}}} - 1\right). \quad (6)$$

Change in actuation balloon length for optimal choice of coil pitch.

The expression of the change in balloon's length is required to derive the robot's speed and turning angle in the next subsections. This change is determined by the maximum and minimum balloon length l_{ai} and l_{av}; thus, we start with the expressions for balloon lengths when fully inflated and deflated:

FIG. 3. Selecting coil pitch to maximize actuation balloon change in length and maximum turning angle configurations. **(A)** Inflated balloon. **(B)** Balloon under vacuum. **(C1)** Two actuation balloons fully inflated and one fully deflated. **(C2)** One actuation balloon fully inflated and two fully deflated. [Larger bending angle occurs in configuration **(C2)**]. **(D)** Projected planar view of configuration **C2** showing 4-bar mechanism with torsional springs at each joint. **(E)** Cross-sectional area around propulsion balloons available for respiration (hatched area, A_p) when robot is straight and travelling through the minimum tube diameter of 11 mm. Shaded area, A_b, is inner lumen of proximal bracing balloon. **(F)** Cross-sectional area around propulsion balloons available for respiration (hatched area, A_p) for maximum turning angle when robot is travelling through the minimum tube diameter of 11 mm. Minimum cross-sectional area occurs for Sections CC and EE at angles $\{0, \beta\}$. On Section DD, the cross-sectional area is the same as in **E**. Color images are available online.

A

diameter, d_a

pitch, p_i

B

$(d_a - d_w)/2$

$d_w/4$

p_i

C

1

2

2

1

1

2

D

l_{ai}

θ_1

θ_2

l_{av}

θ_3

θ_4

β

l'

E

Section BB

Bracing balloon lumen diameter

7.9 mm

A_b

A_p

2.8 mm

11 mm

Minimum tube diameter

Actuation balloon diameter

B

B

F

11 mm

β

$\beta/2$

E

D

C C D

E

Sections CC & EE

Bracing balloon lumen diameter

7.9 mm

2.8 mm

$A_{p,min}$

4.1 mm

11 mm

Minimum tube diameter

Section DD

2.8 mm

A_p

11 mm

Minimum tube diameter

$$l_{ai} = n_i p_i^* + d_w$$
$$l_{av} = n_v p_v^* + d_w$$
(7)

Combining Equations (3), (5), and (7) yields the expression

$$\Delta l^* = l_{ai} - l_{av} = (l_{ai} - d_w)\left[1 - \frac{(d_w + 2t)}{d_a}\sqrt{\frac{\pi^2 + 1}{\pi^2}}\right].$$
(8)

Maximum robot bending angle

Differential inflation of the three actuation balloons causes the robot to bend. This bending angle is not uniform in all directions as shown in Figure 3C but instead exhibits six local maxima corresponding to configurations at which either one or two balloons are fully inflated and the remainder are fully deflated. The bending angle is largest for the three configurations in which two balloons are fully deflated and one is fully inflated (Fig. 3C2).

To develop an analytic expression for this maximum bending angle, we make several assumptions. First, we model the connections between the ends of the actuation balloon and the anchor balloons as elastic flexural joints. Second, we assume that the fully inflated and fully deflated actuation balloons do not buckle and so are straight as shown in Figure 3C. The resulting kinematic structure can be modeled as a planar 4-bar mechanism as shown in Figure 3D in which two sides have length, l', given by

$$l' = \frac{3}{4}d_{bv},$$
(9)

and the remaining two sides have lengths given by the inflated and deflated lengths of the actuation balloons, l_{ai} and l_{av}. The rest configuration of the elastic flexural joints corresponds to $\theta_i = \frac{\pi}{2}$.

Since the robot acts as a 4-bar mechanism, given values for the lengths l_{ai} and l_{av}, there are a family of solutions, $\{\theta_2, \theta_3, \theta_4\} = f(\theta_1)$, where f is a nonlinear function. Modeling the elastic flexural joints as torsional springs, it is possible to solve for the unique configuration that minimizes spring energy. This configuration, derived in the Supplementary Data, results in the actuator balloons being parallel and the 4-bar taking the shape of an isosceles trapezoid. Given this result, the maximum bending angle is

$$\beta = 2\sin^{-1}\left(\frac{\Delta l^*}{2l'}\right)$$
(10)

Combining Equations (9) and (10), it is possible to solve for the change in actuation balloon length that produces a desired maximum bending angle. For example, our distal bracing balloon tube has an outer diameter of 5.2 mm, which is increased slightly by glue thickness to produce an effective $d_{bv} = 5.5$ mm for the actuation balloons. A turning angle of 90° can be produced by $\Delta l^* = 5.8$ mm. While balloon dilations in the bronchi require only a 43° turning angle, robot speed is also proportional to Δl^*. To

ensure that we met our speed specification, we designed our prototype robot with $\Delta l^* = 6.1$ mm. This value corresponds to a maximum bending angle of 95°.

Robot lumen area along actuation balloons

The cross-sectional area of the robot lumen is clearly defined for the bracing balloons by the inner diameter of their tubes and, as described in Bracing Balloon Design section, it can be selected to match the inner diameter of an endotracheal tube to ensure that the open cross section is sufficient for respiration. For the proximal bracing balloon diameter of 7.9 mm, this is given by $A_b = 49$ mm^2.

The cross-sectional area available for respiration along the length of the propulsion balloons is slightly more complicated. It is shown for both the straight and maximally curved robot configurations in Figure 3E and F, respectively. The luminal area of the proximal bracing balloon, A_b, is shaded in Figure 3E.

For the straight configuration (Fig. 3E), the minimum open cross-sectional area (hatch patterned) corresponds to $A_p = 77$ mm^2, which is given by the cross-sectional area of the smallest tube the robot can travel through (11 mm diameter) reduced by the area of the three propulsion balloons (2.8 mm diameter). The value of A_{ps} exceeds A_b indicating that the open cross section around the propulsion balloons is actually larger than is required for respiration.

When the robot is in its maximally curved configuration and moving through a curved tube of minimum diameter (11 mm), as shown in Figure 3F, the open cross section around the propulsion balloons varies between a minimum value, $A_{p,min}$, at angles 0 and β, and a maximum value, A_p, at $\beta/2$. The maximum value (Section DD) is the same as the straight configuration, $A_p = 77$ mm^2. At the minimum values, the plane of the cross section (Sections CC and EE) cuts through the propulsion balloons at an angle as shown in Figure 3F making their cross sections elliptical with minimum and maximum diameters given by d_a and $d_a/\cos(\beta/2)$, respectively. For a maximum bending angle of $\beta = 95°$, the maximum ellipse diameter is 4.1 mm. This results in a minimum open cross section area of $A_{p,min} = 68$ mm^2, which still exceeds the lumen area of the proximal bracing balloon, $A_b = 49$ mm^2.

These results show that both the bracing balloon and propulsion balloon designs provide a sufficient open cross section for respiration.

Results

To validate our analyses and to evaluate the potential of the proposed robot design, we performed five sets of experiments. The first set investigated the analytical criteria developed above for design of the actuation balloons. Next, we constructed a prototype robot and studied the effect of inflation and deflation times, as well as supply pressure on robot speed in rigid tubes and porcine trachea. In the third set of demonstration experiments, we examined three capabilities of the robot. First, we demonstrated that the robot could navigate around corners inside tubes with turning angles equal to the maximum turning angle of the robot. We then explored the clinical potential of the prototype by navigating the robot through *ex vivo* porcine trachea and into the bronchi. These experiments are described below.
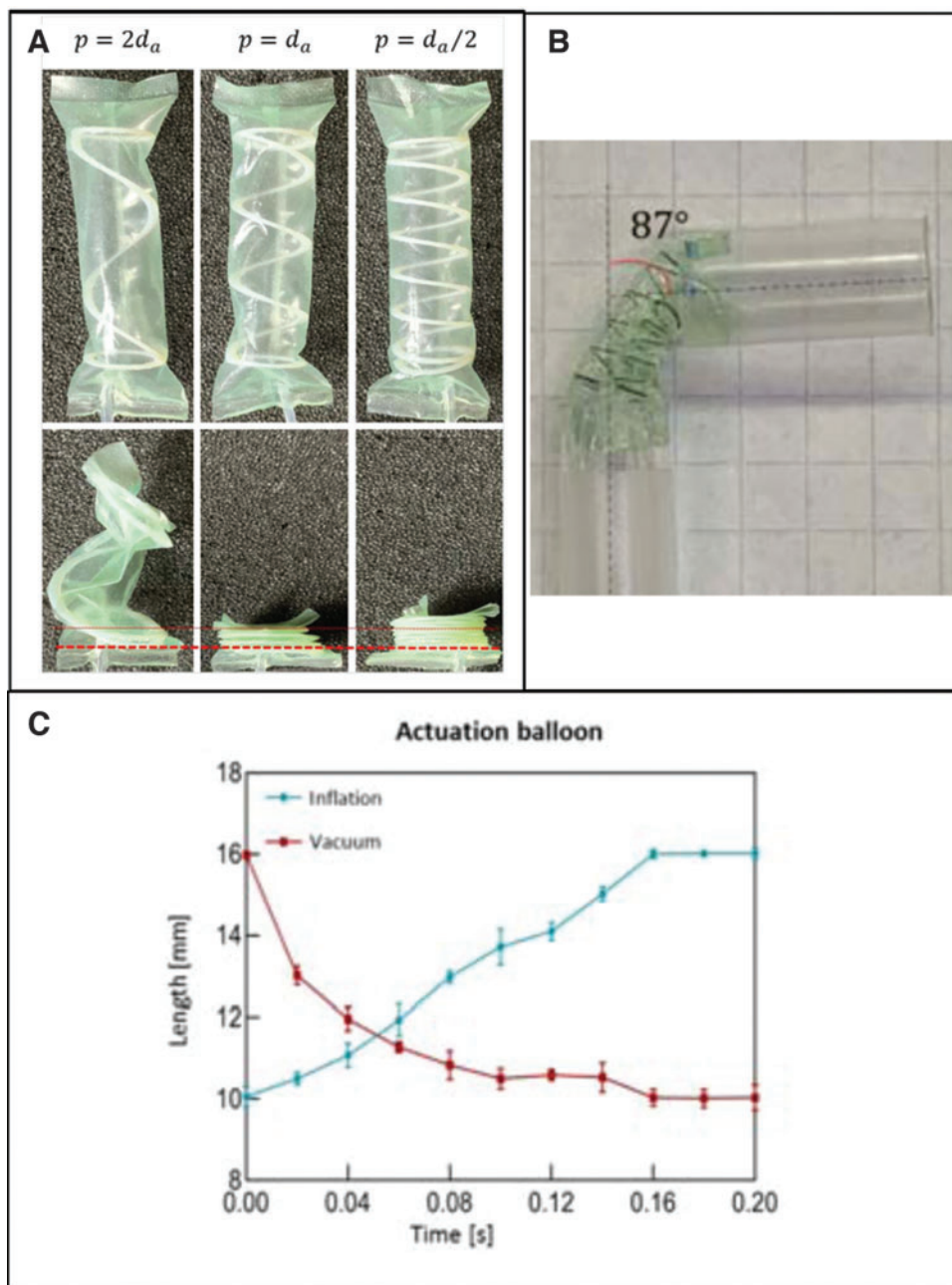
FIG. 4. Balloon and robot evaluation experiments. **(A)** Influence of pitch on minimum balloon length. Diameter = 10 mm, length = 30 mm. **(B)** Maximum bending angle configuration with one balloon fully inflated and two fully deflated. **(C)** Actuation balloon length as a function of inflation and deflation times. Color images are available online.

Evaluation of actuation balloons

We performed experiments to confirm our analytical predictions of optimal helical coil pitch, coil twisting during compression, and maximum bending angle. For our subsequent robot prototype experiments, we also investigated the effect of air pressure on balloon length.

Helical coil pitch versus minimum balloon length. Equation (2) indicates that the minimum balloon length will occur when the helical coil pitch is selected to equal the diameter of the actuation balloon. To validate this equation, we constructed three balloons as shown in Figure 4A with different coil pitches. Each has a diameter of 10 mm and length of 30 mm. As predicted, the coil with a larger pitch (twice the diameter) collapses radially and fails to fully contract. The

balloon with the optimal pitch coil achieves the minimum possible length with the coil fully compressed. Reducing the pitch further, as shown for the third balloon, also prevents radial collapse, but the contracted length is longer since the fully compressed coil is longer.

Maximum bending angle. Our maximum bending angle analysis indicates that the configuration producing the largest angle corresponds to one actuation balloon being fully inflated and the other two being fully deflated as shown in Figure 3C. To validate the energy minimization analysis available as Supplementary Data, we constructed a simplified prototype composed of three actuation balloons attached to the tubes that form the lumens of the bracing balloons (Fig. 4B). The parameters of this prototype match those of

Table 1 with 2.8 mm diameter actuation balloons attached to the outer surface of the distal bracing balloon tubing with a diameter of 5 mm. The measured maximum bending angle of 87° compares favorably with the analytically predicted value of 95°, and it substantially exceeds the 43° needed for balloon dilations in the main human bronchi.

Balloon length as a function of inflation and deflation time. Experiments were conducted to determine the effect of inflation and vacuum time on actuation balloon length. Starting from the fully deflated and inflated states, respectively, the balloons were inflated/deflated for 0–0.2 s. Average length over five trials is plotted in Figure 4C. Both full extension and full compression were achieved in 0.16 s. The value of 0.16 s was used for actuation inflation and deflation times in the speed experiments described below.

Effect of inflation/deflation times and supply pressure on robot speed

As described in Materials and Methods section, a robot prototype was fabricated using the parameters in Table 1. Three sets of experiments were performed. The first set examined the effect of bracing balloon inflation and deflation times on robot speed in a rigid tube. The second set of experiments investigated the effect of increasing inflation pressure on robot speed in both rigid tubes and *ex vivo* swine trachea. The third set examines the effect of rigid tube diameter on robot speed.

Speed-maximizing inflation and deflation times. Robot speed is given by the distance travelled in one locomotion cycle divided by the sum of the balloon inflation and deflation times occurring over the cycle (Fig. 2C). Since speed is proportional to distance travelled, all experiments were conducted using the minimum inflation and deflation times (both 0.16 s) needed to produce the maximum change in length of the actuation balloon. Variations in bracing balloon inflation and deflation time influence how much slip occurs during a cycle. Too short an inflation time can result in too small a frictional propulsive force. Too short a deflation time creates a frictional drag force.

To determine what conditions would maximize speed, experiments were conducted in a clear plastic tube with an inner diameter of 13.5 mm using a supply pressure of 34.5 kPa and vacuum pressure of −62 kPa. Bracing balloon inflation time was varied between 0 and 300 msec, and deflation time was varied between 0 and 400 msec. Three trials were performed for each combination, and speed was calculated using the locomotion distance traveled over 10 propulsion cycles. As shown in Figure 5A, two combinations of inflation and deflation times maximize robot speed. The first occurs for an inflation time of $t_{bi} = 200$ msec and a deflation time of $t_{bv} = 20$ msec. The second occurs for an inflation time of $t_{bi} = 50$ msec and a deflation time of $t_{bv} = 200$ msec.

To understand how these combinations both maximize speed, total robot displacement over the 10 cycles is plotted in Figure 5B. Given that the maximum no-slip displacement of the robot over 10 cycles is 6.1 cm, it can be seen that robot slip occurs for $\{t_{bi}, t_{bv}\} = \{200, 20\}$ msec, but does not for $\{t_{bi}, t_{bv}\} = \{50, 200\}$ msec. At the first maxima, the slip occurs because the short deflation time causes the bracing balloons to fight each other. While it appears contradictory that there is no slip at the second maxima given its short inflation time, this can be understood by examining steps 3–5 of the locomotion cycle in Figure 2C. When the bracing balloon starts inflating in step 3, it continues to inflate in step 4 before the actuation balloon inflating in step 5. In effect, the total inflation time before motion of the actuation balloon is 250 msec, the sum of the bracing balloon inflation and deflation times. Bracing balloon deflation, however, does not experience a similar benefit and so the 20 msec deflation time of the first maxima results in slip.

Effect of inflation pressure on robot speed. While it is desirable in clinical applications to limit the balloon inflation pressures during locomotion, experiments were performed to gain an understanding of how increasing supply pressure affects robot speed. Deflation pressure is maintained at the maximum value and not varied in these experiments since there is no clinical benefit in reducing it. Experiments were performed using inflation pressures of 34.5–55.2 kPa in a 13.5 mm inner diameter rigid plastic tube and in an *ex vivo* swine trachea. The tracheal cross section was oval and varied between 12 mm by 13 mm at one end to 11 mm by 12 mm at the other end. Bracing balloon deflation times of $t_{bv} = \{20, 200\}$ msec were used, corresponding to the two speed maxima identified above. Bracing balloon inflation time, t_{bi}, was varied between 0 and 300 msec.

Plastic tube. Speed and displacement are plotted versus inflation time in Figure 5C and D. Recall that for a 20 msec deflation time, while some slip occurred, a 200 msec inflation time produced a speed maxima of 7 mm/s (Fig. 5A) with shorter inflation times reducing the total displacement from over 5 to 1 cm or less (Fig. 5B).

FIG. 5. Robot speed and displacement as a function of bracing balloon inflation/deflation times and inflation pressure. **(A)** Robot speed versus bracing balloon inflation/deflation time in a 13.5 mm diameter plastic tube with 34.5 kPa inflation pressure. **(B)** Robot displacement over 10 propulsion cycles versus bracing balloon inflation/deflation time in a 13.5 mm diameter plastic tube with 34.5 kPa inflation pressure. **(C)** Robot speed versus bracing balloon inflation time as a function of pressure in a 13.5 mm diameter plastic tube. **(D)** Robot displacement over 10 propulsion cycles versus bracing balloon inflation time as a function of pressure in a 13.5 mm diameter plastic tube. **(E)** Robot speed versus bracing balloon inflation time as a function of pressure for a deflation time of 200 msec in *ex vivo* swine trachea. **(F)** Robot displacement over 10 propulsion cycles versus bracing balloon inflation time as a function of pressure for a deflation time of 200 msec in *ex vivo* swine trachea. **(G)** Robot speed versus bracing balloon inflation time as a function of tube diameter for a deflation time of 200 msec and inflation pressure of 34.5 kPa. **(H)** Robot displacement over 10 propulsion cycles versus bracing balloon inflation time as a function of tube diameter for a deflation time of 200 msec and inflation pressure of 34.5 kPa. Each experiment was repeated thrice. Standard deviation is shown using error bars. Color images are available online.
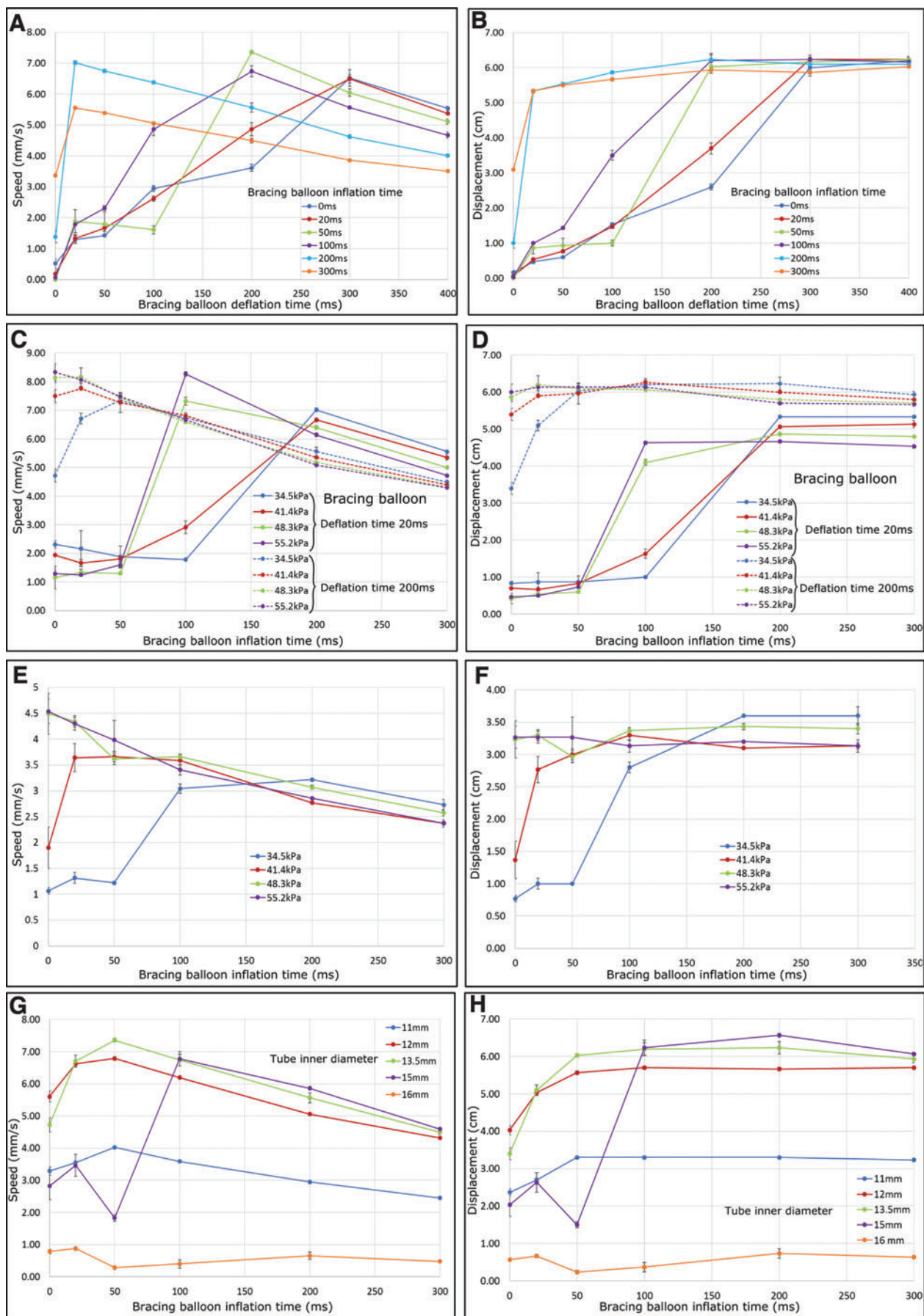
Higher inflation pressures lead to faster filling of the bracing balloons. As shown in Figure 5C (solid lines), this shifts the velocity peak at pressures of 48.3 and 55.2 kPa to the smaller inflation time of 100 msec. From Figure 5D, this timing slightly reduces total displacement, that is, there is more slip, but the shorter inflation time leads to higher speeds with 55.2 kPa producing over 8 mm/sec. In contrast, for larger inflation times, higher pressures slightly increase slip and reduce velocity since higher pressures require longer deflation times.

Considering now the second speed maxima produced for a bracing balloon deflation time of $t_{bv} = 200$ msec, it can be observed from Figure 5C and D (dashed lines) that varying pressure produces similar effects as for the shorter deflation time. The most significant effect occurs at low inflation times for which the higher inflation pressures fill the bracing balloons faster leading to less slip and higher speeds. The highest speed of over 8 mm/s occurs for an inflation time of 0 msec. (Note that total bracing balloon inflation time before actuation balloon inflation/deflation is the sum of bracing balloon inflation and deflation time.)

In summary, increasing inflation pressure can increase velocity by enabling shorter bracing balloon inflation times to be used.

Ex vivo trachea.   Recall that in the dry rigid tube, two sets of conditions produced speed maxima. In the first, short inflation and deflation times created some slip between the robot and the tube, but the short cycle time resulted in high speeds. The second maxima corresponded to using the shortest inflation and deflation times that produced minimal slip.

In contrast with the dry rigid tube, the freshly harvested swine trachea had an inner surface that was wet, slippery, and compliant. These conditions created so much slip for a deflation time of 20 msec that no speed maxima was observed, and robot speed was well below our 2 mm/sec target for all inflation times and pressures.

As shown in Figure 5E and F, however, the second speed maxima associated with minimizing slip was effective in the trachea. Using a 200 msec deflation time, slip does occur (3 cm displacement vs. 6 cm in the plastic tube), but this displacement is sufficient to produce robot speeds greater than our speed specification of 3 mm/sec for most inflation times and pressures. For an inflation time of 50 msec, increasing pressure above 34.5 kPa decreases slip, but otherwise variations in pressure produce little effect on robot displacement and speed.

Effect of tube diameter on robot speed.   To understand the effect that tube diameter has on robot speed, we performed experiments using plastic tubes with different inner diameters. These experiments used the 200 msec-deflation-time speed maxima corresponding to minimizing slip and a pressure of 34.5 kPa. The smallest diameter tube that the proximal bracing balloon could fit inside was 11 mm diameter, so the set of diameters tested was {11,12,13.5,15,16} mm. These results are plotted in Figure 5G and H.

Recalling that the anchor balloons were designed for navigation through tubes of 11–15 mm diameter, it can be observed that this design specification was achieved. For the diameter range of 12–15 mm, little to no slip occurs for inflation times of 100 msec or greater and robot speeds exceed 6 mm/sec.

Slip increases and speed decreases for diameters outside this range. For example, the robot fits snugly inside an 11 mm diameter tube when the bracing balloons are deflated. This creates a drag force that reduces displacement and speed by a factor of two. At the other extreme, when the tube diameter is greater than or equal to the inflated diameter of the bracing balloons (16 mm), the robot is unable to generate sufficient propulsion force.

Robot navigation experiments

To evaluate the capability of the system to navigate through branching tubes and in the context of endoscopic clinical procedures, we performed three experiments. The first experiment evaluated the capability to navigate around corners in rigid tubes. In the second experiment, we evaluated the ability of the robot to navigate through *ex vivo* swine trachea and into the bronchi.

Navigating around corners.   While the robot has a clinical specification for a maximum turning angle of 43° from the trachea into the left main bronchus, the actuation balloons were designed for 90° turns. To validate whether or not the robot could propel itself through a tube while making these turns, we constructed the three-way tube junction (inner diameter 13.5 mm, 45° and 90° turns) shown in Figure 6A. A three-way junction was used because it requires the robot to be steered into the desired branch. Navigation experiments were performed using an actuation pressure of 34.5 kPa and bracing balloon inflation and deflation times of {50,200} msec.

Using the game controller, the locomotion cycle is preprogrammed for straight motion and for turning motions. When the junction was approached, the controller was used to steer the robot tip into the desired branch. Once the tip had entered the desired branch, the straight motion cycle could be used to complete navigation into the branch. As shown in Supplementary Video S1, the robot was easily able to navigate both the 45° and 90° turns.

One challenge to turning 90° results from the robot bending angle not being symmetric about its axis (Fig. 3C). The three configurations of maximum bending angle are located 60° apart. If the maximum bending angle is needed to enter a side branch, but the robot body is rotated such that the maximum is not aligned with the side branch, the robot cannot directly enter the side branch. To rotate the robot into alignment, we developed a two-step strategy. First, all balloons are deflated and the robot is retracted a fixed distance by pulling its tether. Second, the robot is locomoted forward causing it to rotate about its axis. Since the rotation per locomotion cycle can be estimated during initial navigation, the retraction distance can be computed based on the alignment error.

Navigation of *ex vivo* porcine trachea and bronchi.   The goal of this experiment was to demonstrate that the robot could navigate to the location in the bronchi where balloon dilations are performed to relieve occlusions that can occur
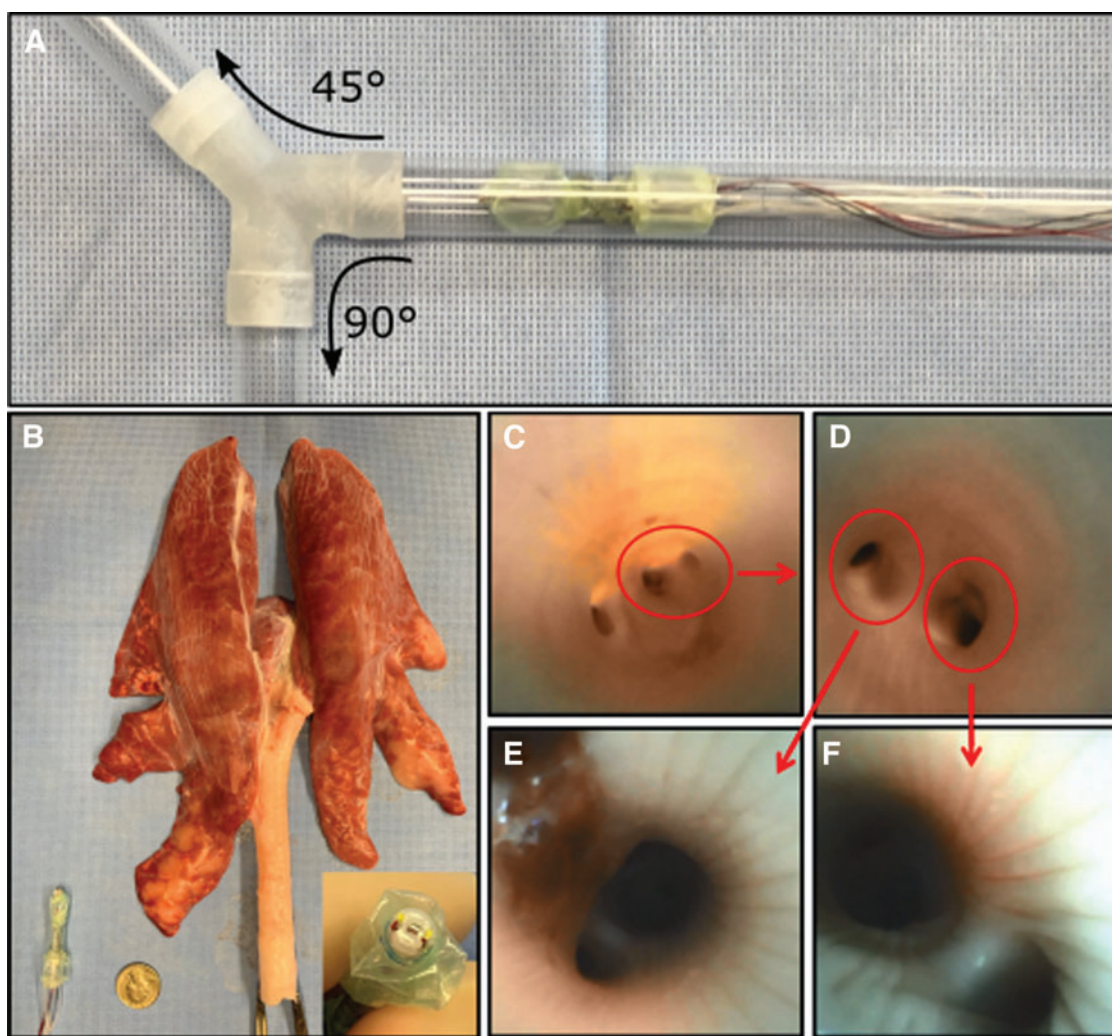
FIG. 6. Robot navigation experiments. **(A)** Three-way tube junction (inner diameter of 13.5 mm) with 45° and 90° turns. (Supplementary Video S1.) **(B)** *Ex vivo* porcine trachea and lungs with robot. Inset showing camera on robot tip. (Supplementary Video S2.) **(C)** Robot view inside trachea showing three porcine bronchi. **(D)** Robot view of caudal lobe bronchi. **(E)** Robot view from inside right caudal lobe bronchus showing subsequent branches. **(F)** Robot view inside left caudal lobe bronchus showing distal branches. Color images are available online.

after lung transplantation. We also wished to validate that robot locomotion would not damage the tissue and to demonstrate that the robot could be used to inspect the regions just distal to these locations to determine tissue health.

The *ex vivo* experiment was performed in the trachea and lungs of a 40 kg Yorkshire pig (Fig. 6B). The robot was placed inside the trachea. Using the game controller, the robot was navigated using video guidance to the carina where the trachea divides into the bronchi. While humans have two bronchi, pigs have three as shown in Figure 6C. The robot was sequentially navigated successfully into the left and right caudal lobe bronchi as identified in Figure 6C and D. Inside each bronchus, the robot was navigated to the location of its distal branches (Fig. 6E, F, and Supplementary Video S2). Thus, the robot was able to reach the locations where balloon dilations would be performed. Before and after conducting the locomotion experiments, we inspected the *ex vivo* porcine tracheal tissue and no damage was noted.

Conclusion

This article proposes a soft robot design that combines the functionalities of endoscopic visualization and balloon dilation. This eliminates the visual occlusion problems that arise due to using separate instruments. It also provides the capability to see around corners, which currently cannot be achieved with the straight rigid endoscopes that are most often used in the airways. The robot is powered by pressurized air and vacuum sources that are found in standard clinical procedure rooms. Since the design is based on balloon catheter technology, clinical versions of the device can be easily manufactured by medical balloon catheter fabricators. The robot design is also sufficiently inexpensive to be used as a disposable ($131 including the chip camera and LED mounted on its tip).

The prototype presented in this article is intended for navigation in the human bronchi and trachea. The specifications

for this application are that the robot be able to: (1) navigate through lumens with diameters of 11–16 mm, (2) achieve speeds of 3 mm/sec, and (3) perform turns up to 43°. We designed the robot for a slightly smaller range of lumens 11–15 mm in diameter to ensure that it could enter the smaller swine bronchi that we used for testing. We also increased the turning angle specification used for design to 90°.

In our evaluation experiments, the robot was able to move at speeds greater than 3 mm/sec in plastic tubes of diameters between 11 and 15 mm with top speeds exceeding 7 mm/sec. In *ex vivo* swine trachea with a minimum diametral dimension varying between 11 and 12 mm, robot speed also exceeded 3 mm/sec. While we were not able to test the robot in larger trachea, our results with larger rigid tubes suggest that the robot will be capable of achieving the desired speed in these larger sizes.

In *ex vivo* swine lungs, we demonstrated that the robot could turn into the bronchi to reach the locations where dilations associated with lung transplantation would occur. We also evaluated turning inside rigid tubes and demonstrated that the robot can perform both 45° and 90° turns.

To evaluate robot safety, we investigated the effect of inflation pressure on robot performance. We demonstrated that 34.5 kPa inflation pressure was sufficient to meet the lumen diameter and speed specifications. Furthermore, the swine tracheal tissue used in our tests was examined for damage due to the bracing balloons pressing and sliding against the walls, and none was observed for inflation pressures in the tested range of 34.5–55.2 kPa. Consequently, higher inflation pressures could likely be used safely to produce further increases in robot speed. In addition, it was observed that no pinching of the tissue occurred during contraction of the actuation balloons.

Our experiments revealed two different locomotion regimes that locally maximized robot speed in dry rigid tubes. The top speed for both regimes was just over 7 mm/sec in a 13.5 mm diameter tube. The first regime uses short inflation and deflation times for the bracing balloons such that they experience some slip against the tube walls and move only about 5 mm out of a no-slip maximum of 6.1 mm. Despite the slip, the short cycle time produces a local speed maxima. The second speed maxima occurs when the inflation and deflation times are just long enough that no slip occurs between the bracing balloons and the walls.

Experiments in the slippery compliant conditions of an *ex vivo* swine trachea revealed that this latter technique was the only way to maximize speed. In this case, however, slip cannot be eliminated, but only minimized with displacements per cycle of about 3.5 mm out of the maximum 6.1 mm.

The article also provides several analytical contributions related to the design of linearly expanding balloons with internal helical coils to prevent radial collapse. Specifically, we derived and demonstrated how selection helical coil pitch equal to balloon diameter maximizes stroke length. We also derived and demonstrated the maximum turning angle that can be achieved using a robot bending section composed of three of these balloons.

Future work is needed to assess the safety of the interaction between the robot and airway tissue. This would best be investigated through in vivo navigation experiments performed in sheep or pigs sized to match the human airways. Such experiments could involve demonstrating the capability to navigate into and out of the main bronchi while inflating the bracing balloons to different diameters or pressures. Subsequently, the tissue could be assessed visually, as well as by histological techniques, to check for damage.

Author Disclosure Statement

No competing financial interests exist.

Supplementary Material

Supplementary Data

References

1. Benninger MS, Ferguson BJ, Hadley JA, *et al.* Adult chronic rhinosinusitis: definitions, diagnosis, epidemiology, and pathophysiology. Otolaryngol Head Neck Surg 2003; 129:S1–S32.
2. Minni A, Dragonetti A, Sciuto A, *et al.* Use of balloon catheter dilation vs. traditional endoscopic sinus surgery in management of light and severe chronic rhinosinusitis of the frontal sinus: a multicenter prospective randomized study. Eur Rev Med Pharmacol Sci 2018;22:285–293.
3. Alraiyes AH, Inaty H, Machuzak MS. Vanishing bronchus after lung transplantation: the role of sequential airway dilatations. Ochsner J 2017;17:71–75.
4. Yuen MT, Tsang RK, Wong IY, *et al.* Long-term pharyngeal dysphagia after esophagectomy for esophageal cancer—an investigation using videofluoroscopic swallow studies. Dis Esophagus 2019;32:doy068.
5. Mi W, Zhang C, Wang H, *et al.* Measurement and analysis of the tracheobronchial tree in Chinese population using computed tomography. PLoS One 2015;10:e0123177.
6. Farrow S, Farrow C, Soni N. Size matters: choosing the right tracheal tube. Anaesthesia 2012;67:815–822 Editorial.
7. Liang K, Traverso G, Lee HC, *et al.* Ultrahigh speed en face OCT capsule for endoscopic imaging. Biomed Opt Express 2015;6:1146–1163.
8. Sharma SD, Gupta SL, Wyatt M, *et al.* Safe balloon sizing for endoscopic dilatation of subglottic stenosis in children. J Laryngol Otol 2017;131:268–272.
9. Ciuti G, Caliò R, Camboni D, *et al.* Frontiers of robotic endoscopic capsules: a review. J Microbio Robot 2016;11:1–8.
10. Cosentino F, Tumino E, Passoni GR, *et al.* Functional evaluation of the endotics system, a new disposable self-propelled robotic colonoscope: in vitro tests and clinical trial. Int J Artif Organs 2009;32:517–527.
11. Bernth JE, Arezzo A, Liu H. A novel robotic meshworm with segment-bending anchoring for colonoscopy. IEEE Robot Autom Lett 2017;2:1718–1724.

12. Connolly F, Polygerinos P, Walsh CJ, *et al.* Mechanical programming of soft actuators by varying fiber angle. Soft Robot 2015;2:26–32.

13. Takeshima H, Takayama T. Geometric estimation of the deformation and the design method for developing helical bundled-tube locomotive devices. IEEE/ASME Trans Mechatron 2017;23:223–232.

14. Ozaki K, Wakimoto S, Suzumori K, *et al.* Novel design of rubber tube actuator improving mountability and drivability for assisting colonosocope insertion. In: 2011 IEEE International Conference on Robotics and Automation (ICRA), Shanghai, China, May 9–13. Piscataway, NJ: IEEE, 2011, pp. 3263–3268.

15. Adachi K, Yokojima M, Hidaka Y, *et al.* Development of endoscopic robot and experiment in the large intestine of dead swine. In: 2011 IEEE International Conference on Robotics and Biomimetics (ROBIO), Karon Beach, Phuket, Thailand, December 7–11. Piscataway, NJ: IEEE, 2011, pp. 467–472.

16. Lim J, Park H, Moon S, *et al.* Pneumatic robot based on inchworm motion for small diameter pipe inspection. In: 2007 IEEE International Conference on Robotics and Biomimetics (ROBIO), Sanya, China, December 15–18. Piscataway, NJ: IEEE, 2007, pp. 330–335.

17. Zhang B, Fan Y, Yang P, *et al.* Worm-like soft robot for complicated tubular environments. Soft Robot 2019;6:399–413.

18. Manfredi L, Capoccia E, Ciuti G, Cuschieri A. A Soft Pneumatic Inchworm Double balloon (SPID) for colonoscopy. Sci Rep 2019;9:11109.

19. Heung H, Chiu PWY, Li Z. Design and prototyping of a soft earthworm-like robot targeted for GI tract inspection. In: 2016 IEEE International Conference on Robotics and Biomimetics (ROBIO), Qingdao, China. Piscataway, NJ: IEEE, 2016, pp. 497–502.

20. Wang K, Ge Y, Jin X. A micro soft robot using inner air transferring for colonoscopy. In: 2013 IEEE International Conference on Robotics and Biomimetics (ROBIO), Shenzhen, China. Piscataway, NJ: IEEE, 2013, pp. 1556–1561.

21. Qin L, Liang X, Huang H, *et al.* A versatile soft crawling robot with rapid locomotion. Soft Robot 2019;6:455–467.

22. Robertson MA, Paik J. New soft robots really suck: vacuum-powered systems empower diverse capabilities. Sci Robot 2017;2:eaan6357.

23. Alazmani A, Hood A, Jayne D, *et al.* Quantitative assessment of colorectal morphology: implications for robotic colonoscopy. Med Eng Phys 2016;38:148–154.

Address correspondence to:
Pierre E. Dupont
Department of Cardiovascular Surgery
Boston Children's Hospital
Harvard Medical School
Harvard University
Boston, MA 02115
USA

E-mail: pierre.dupont@childrens.harvard.edu